# Chapter 4

# Investigation on $Al^{3+}$ ion storage in $Bi_2MoO_6$ and $Bi_2WO_6$ for rechargeable aqueous aluminum-ion battery

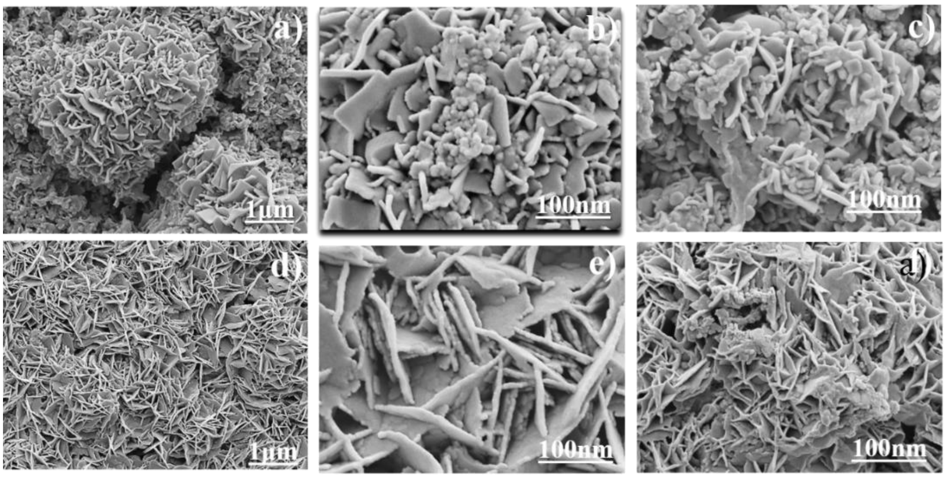

Reversible and stable electrochemical $Al^{3+}$ ion storage process defines the functioning of a rechargeable aluminum-ion battery. This chapter illustrates the electrochemistry of $Bi_2MoO_6$ and $Bi_2WO_6$ for $Al^{3+}$ ion storage in aqueous electrolyte. A mechanistic study reveals probable transformation of $Bi_2WO_6$ to BiOCl during the electrochemical process.

*Ref.: R. Baishya, H. Phukon, D. Kalita, S. R. Barman, and S. K. Das, "Investigation on $Al^{3+}$ ion storage in $Bi_2MoO_6$ and $Bi_2WO_6$ for rechargeable aqueous aluminum-ion battery," Journal of Energy Storage, vol. 94, p. 112 541, 2024.*

# 4. Investigation on $Al^{3+}$ ion storage in $Bi_2MoO_6$ and $Bi_2WO_6$ for rechargeable aqueous aluminum-ion battery

## 4.1 Introduction

In continuation of the previous chapters, it is to be noted that there is another set of two-dimensional Bi compounds such as $Bi_2MoO_6$ and $Bi_2WO_6$. These materials also belong to the aurivillous family with a general formula $Bi_2A_{n-1}B_nO_{3n+1}$ (where A = Ca, Sr, Ba, Pb, Na, K and B = Ti, Nb, Ta, Mo, W, Fe). The crystal structure consists of layered oxide layers of $(Bi_2O_2)^{2+}$ sheets which are sandwiched between $(A_{n-1}B_nO_{3n+1})^{2-}$ layers which provides a stable and an open channel for ion insertion [1,2]. There are reports of $Bi_2MoO_6$ and $Bi_2WO_6$ for various applications such as photocatalytic activity, sensing, ferroelectric, pyroelectric and supercapacitor devices [3-9]. All of these fascinating features encourage us to carry out an electrochemical investigation on $Bi_2MoO_6$ and $Bi_2WO_6$ for $Al^{3+}$ ion storage in aqueous media. To the best of my knowledge, this kind of study for both these materials has hitherto been unknown.

## 4.2 Experimental Section

### 4.2.1 Materials

Bismuth nitrate pentahydrate (Bi $(NO_3)_3.5H_2O$, Sigma Aldrich), sodium molybdate ($Na_2MoO_4$, Sigma Aldrich), sodium tungstate ($Na_2WO_4$, Sigma Aldrich), ethanol and distilled water.

### 4.2.2 Synthesis

$Bi_2MoO_6$ was prepared using a hydrothermal technique as reported in ref [10]. Briefly, 3.5 mmol of $Bi(NO_3)_3.5H_2O$ and 1.75 mmol of $Na_2MoO_4$ were dissolved in 10 mL of ethylene glycol under constant magnetic stirring. The solution was mixed with 20 mL of ethanol and stirred for 5 hours to get a homogeneous mixture. Then the solution was transferred to a teflon lined autoclave and it was heated at 160 °C for 16 h. After letting it to cool naturally, the solution was washed with ethanol and distilled water several times. The obtained sample was dried at 80 °C overnight to get the final product. Exactly similar method was adopted in order to synthesize $Bi_2WO_6$. The tungsten precursor in this case is $Na_2WO_4$.

### 4.2.3 Characterization

The phases and purity of the prepared samples were identified using X- ray diffraction (BRUER AXS D8 FOCUS, Cu-$K_\alpha$ radiation, $\lambda$= 1.5406 Å) and Raman spectroscopy (RENISHAW BASIS SERIES WITH 515 LASER, RENISHAW, UK). FESEM technique (JEOL-JSM7200F) was used to understand the morphology. XPS analysis was performed to investigate the surface chemical composition using ESCALAB $Xi^+$ system.

### 4.2.4 Electrochemical analysis

To fabricate the working electrode for the electrochemical analysis, electrode slurries were prepared using the active materials ($Bi_2MoO_6$/$Bi_2WO_6$), carbon black and polyvinylidene fluoride in a weight ratio of 7:2:1 using N-methyl-2-pyrrolidone as solvent. The obtained slurry was cast on a graphite piece and it was dried at 90 °C for 12 hours. The electrochemical activities of $Bi_2MoO_6$/$Bi_2WO_6$ were investigated using cyclic voltammetry (CV) and galvanostatic charge-discharge experiments in a three-electrode glass cell set up with Pt and Ag/AgCl were used as counter and reference electrodes respectively. The CV analysis was performed in the potential window of -0.8 V to 0.4 V (vs Ag/AgCl) at different scan rates. Similarly, the charge-discharge profiles for both the materials were performed in the same voltage range at different current densities ranging from 0.5 to 2.5 $Ag^{-1}$. The electrolytes used were of various concentration of $AlCl_3$ and $Al_2(SO_4)_3$. Electrochemical impedance spectroscopy (EIS) was performed in the frequency range of 1 mHz to 200 kHz with a signal amplitude of 10 mV.

## 4.3 Results and Discussion

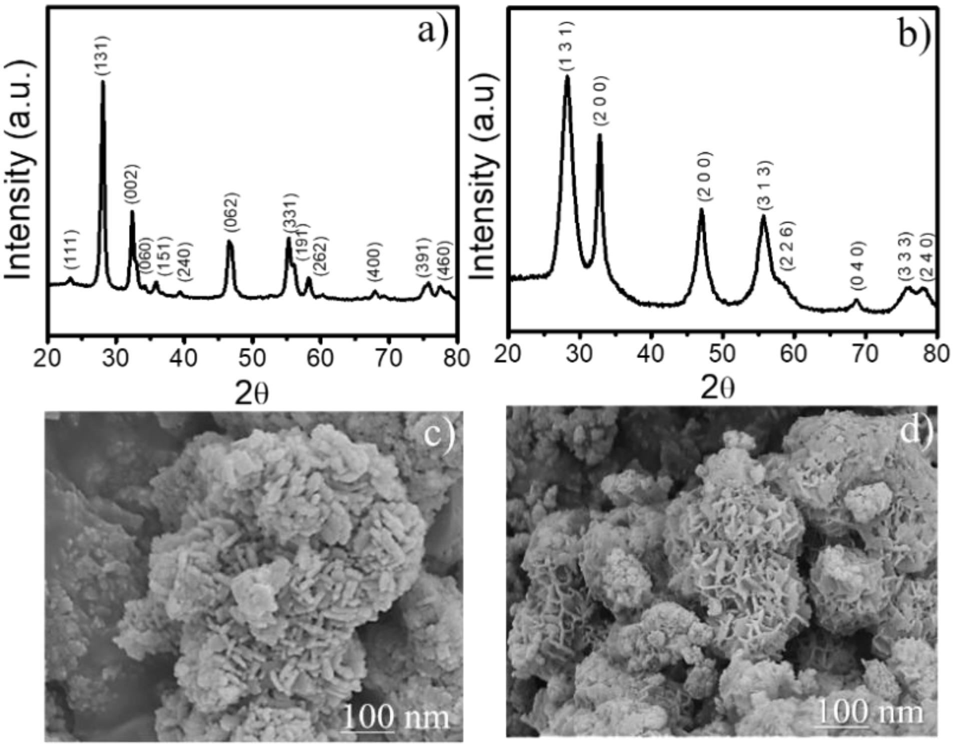

**Figure 4.1** XRD patterns (a) $Bi_2MoO_6$ and (b) $Bi_2WO_6$, FESEM image of (c) $Bi_2MoO_6$ and (d) $Bi_2WO_6$.

The X-ray diffraction patterns of $Bi_2MoO_6$ and $Bi_2WO_6$ are shown in figure 4.1. The diffraction peaks obtained for $Bi_2MoO_6$ (figure 4.1a) and $Bi_2WO_6$ (figure 4.1b) match well with the orthorhombic phase (JCPDS No.– 84-0787 & JCPDS No. -73-2381). FESEM images indicate the formation of clusters of nanoflakes in both cases (Figure 4.1(c, d)).

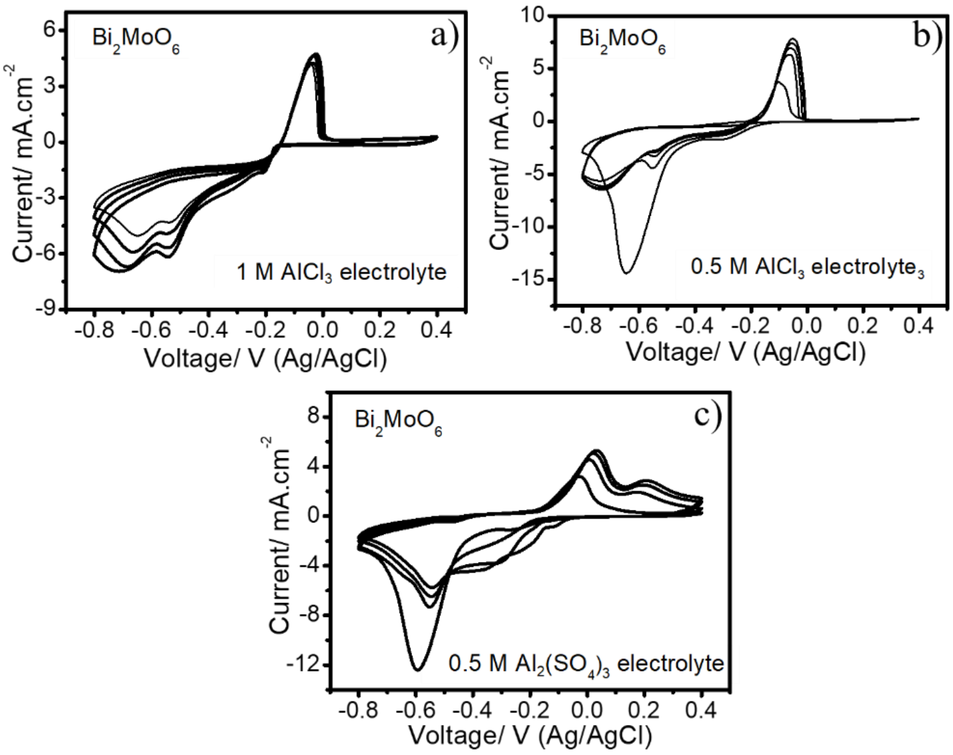

**Figure 4.2** CV profiles of $Bi_2MoO_6$ (a) 1 M $AlCl_3$, (b) 0.5 M $AlCl_3$ and (c) 0.5 M $Al_2(SO_4)_3$ aqueous electrolyte at a scan rate of 2.5 mVs$^{-1}$.

The initial electrochemical assessment of $Bi_2MoO_6$ and $Bi_2WO_6$ was performed by cyclic voltammetry in $AlCl_3$ and $Al_2(SO_4)_3$ containing aqueous electrolytes of different concentrations in the potential range of -0.8 V to 0.4 V at a scan rate of 2.5 mVs$^{-1}$. Figure 4.2a shows the CV profiles of $Bi_2MoO_6$ in 1 M $AlCl_3$ aqueous electrolyte which apparently shows prominent redox activity. There are two cathodic peaks located at -0.54 V and -0.67V which are observed for all cathodic scans, whereas only single but intense anodic peak could be observed at -0.03 V in all the anodic scans. Similar electrochemical activity is also observed for 0.5 M $AlCl_3$ aqueous electrolyte (Figure 4.2b). On the other hand, as shown in figure 4.2c, the CV profiles attained in 0.5 M $Al_2(SO_4)_3$ aqueous electrolyte show slightly different behavior. First, there is only one very intense cathodic peak at -0.6 V in the 1st cathodic scan. In the subsequent cathodic cycles, however, there is emergence of two cathodic peaks around -0.4 V and -0.55 V. Second, two prominent anodic peaks around 0.03 V and 0.22 V could be noticed in all the anodic scans except the first scan.

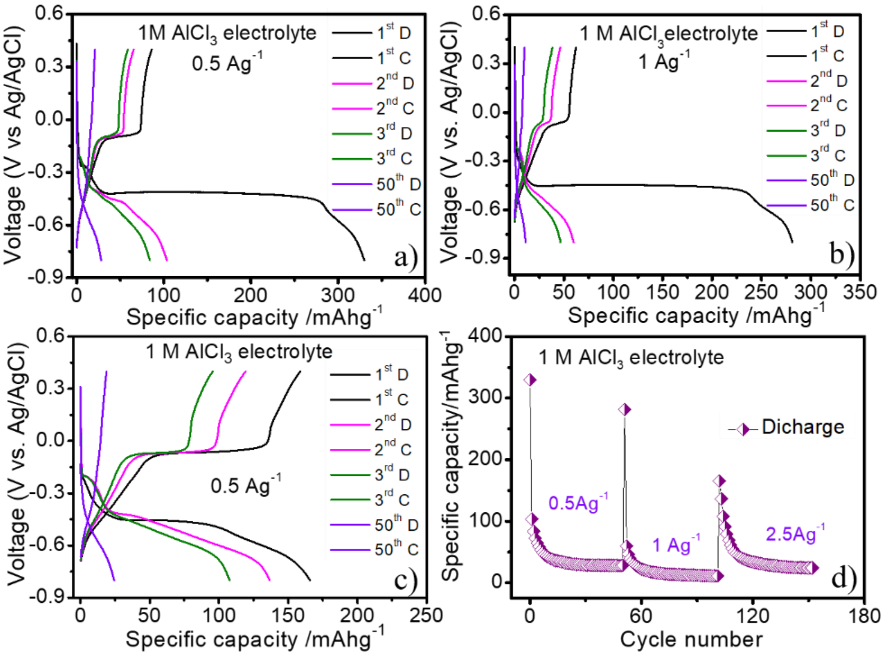

**Figure 4.3** Galvanostatic charge discharge profiles of $Bi_2MoO_6$ in 1 M $AlCl_3$ at a current density of (a) 0.5 $Ag^{-1}$, (b) 1 $Ag^{-1}$ and c) 2.5 $Ag^{-1}$; c) Rate capability of $Bi_2MoO_6$ at different current densities in 1 M aqueous $AlCl_3$ electrolyte.

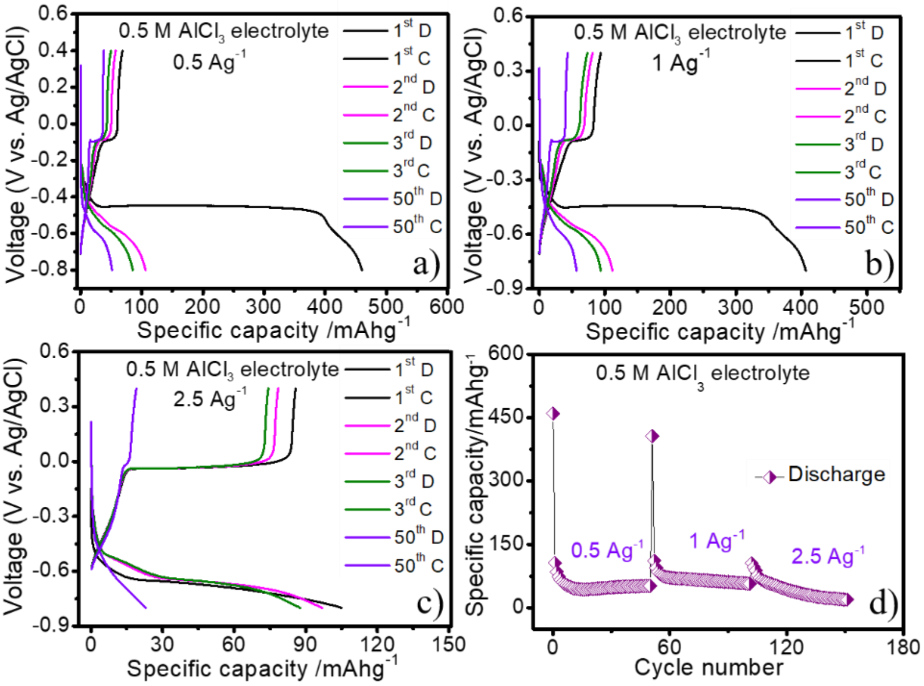

**Figure 4.4** Galvanostatic charge discharge profiles of $Bi_2MoO_6$ at a current density of (a) 0.5 $Ag^{-1}$, (b) 1 $Ag^{-1}$ and c) 2.5 $Ag^{-1}$; c) Rate capability of $Bi_2MoO_6$ at different current densities in 0.5 M aqueous $AlCl_3$ electrolyte.

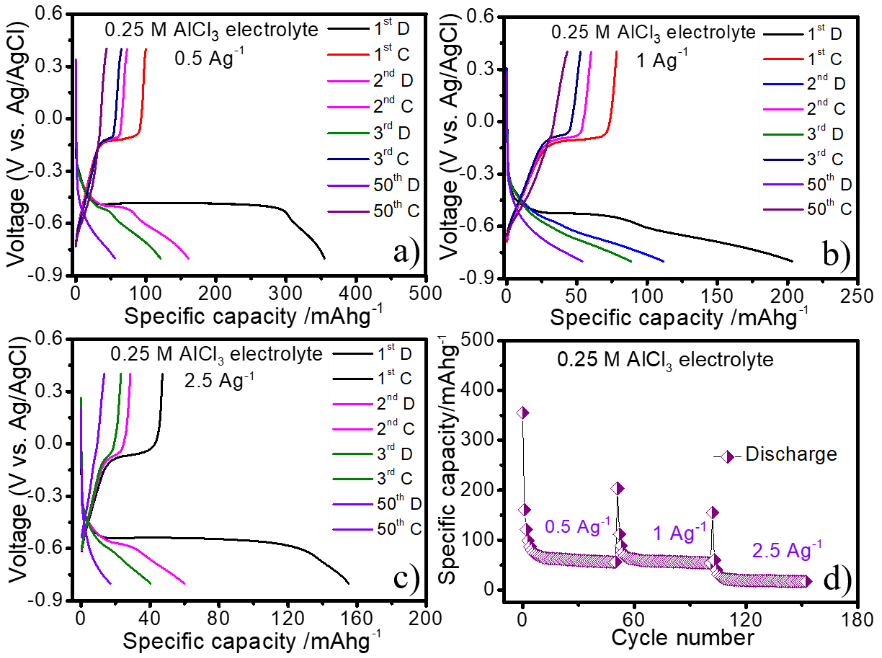

**Figure 4.5** Galvanostatic charge discharge profiles of $Bi_2MoO_6$ at a current density of (a) 0.5 $Ag^{-1}$, (b) 1 $Ag^{-1}$ and c) 2.5 $Ag^{-1}$; c) Rate capability of $Bi_2MoO_6$ at different current densities in 0.25 M aqueous $AlCl_3$ electrolyte.

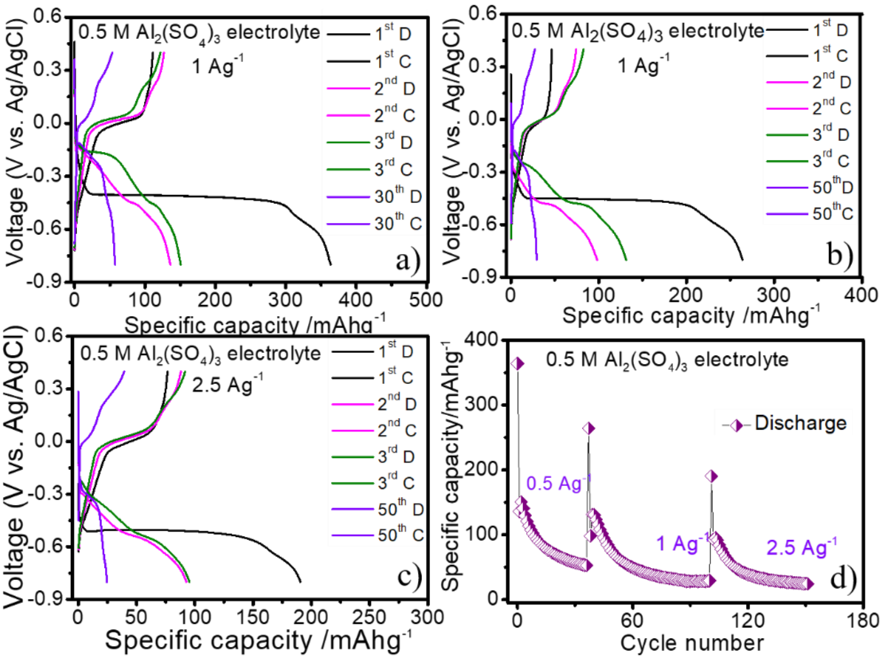

**Figure 4.6** Galvanostatic charge discharge profiles of $Bi_2MoO_6$ at a current density of (a) 0.5 $Ag^{-1}$, (b) 1 $Ag^{-1}$ and c) 2.5 $Ag^{-1}$; d) Rate capability of $Bi_2MoO_6$ at different current densities in 0.5 M $Al_2(SO_4)_3$ aqueous electrolyte.

The galvanostatic charge-discharge (GCD) profiles of $Bi_2MoO_6$ also support the outcome of cyclic voltammetry measurements. Figure 4.3a shows the GCD profiles of $Bi_2MoO_6$ in 1 M $AlCl_3$ aqueous electrolyte in the potential range of -0.8 V to 0.4 V (vs. Ag/AgCl) at a specific current rate of 0.5 Ag$^{-1}$. There is a prominent discharge potential plateau at -0.4 V and a charge plateau at -0.1 V in the initial cycle. Since there is capacity fading, the potential plateaus are not clearly visible after the first discharge cycle. The estimated initial discharge and charge capacity values are 330 mAhg$^{-1}$ and 86 mAhg$^{-1}$ respectively. Almost similar trend was also observed for higher current densities (figure 4.3c). Since 1 M $AlCl_3$ aqueous electrolyte is highly acidic, GCD measurements were carried out at 0.5 M and 0.25 M $AlCl_3$ electrolyte. The charge-discharge profiles in this case (figure 4.4 and 4.5) are almost identical to the profiles obtained with 1 M $AlCl_3$ electrolyte. However, a slight improvement in stability could be noticed (figure 4.4). On the other hand, when evaluated in 0.5 M $Al_2(SO_4)_3$ aqueous electrolyte at the same current density, the initial discharge profile shows a prominent discharge potential plateau at -0.4 V and a charge plateau at -0.1 V (figure 4.6a). However, the most prominent discharge potential plateau is observed at -0.2 V from the second discharge cycle onwards with minor plateau at -0.4 V. This behaviour is consistent at higher current density also (figure 4.6c). Although there is capacity decline in this case also (figure 4.6d), but the decline is more severe in the case of $AlCl_3$ electrolyte.

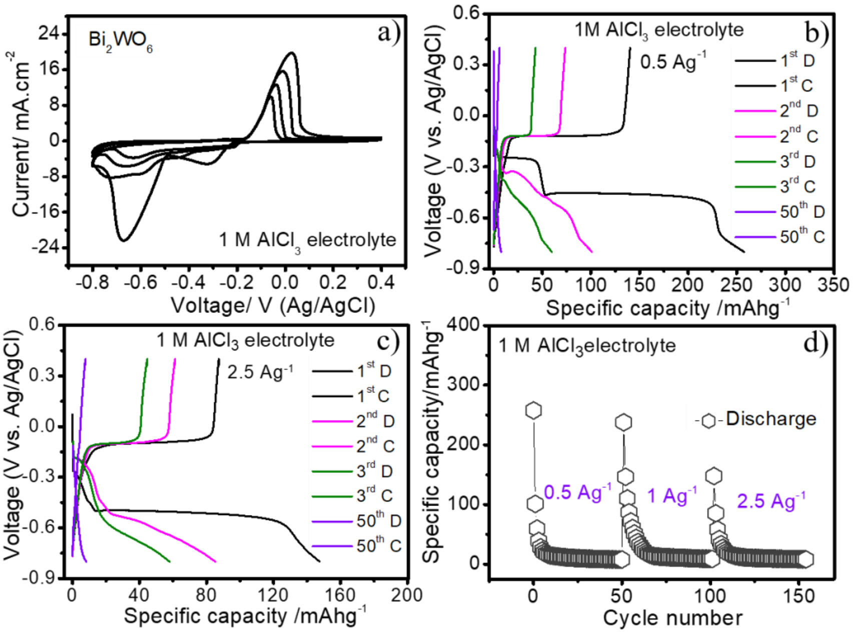

**Figure 4.7** (a) CV profile, Galvanostatic charge discharge profiles of $Bi_2WO_6$ at a current density of (b) 0.5 Ag$^{-1}$ and (c) 2.5 Ag$^{-1}$; (d) Rate capability of $Bi_2WO_6$ at different current densities in 1 M aqueous $AlCl_3$ electrolyte.

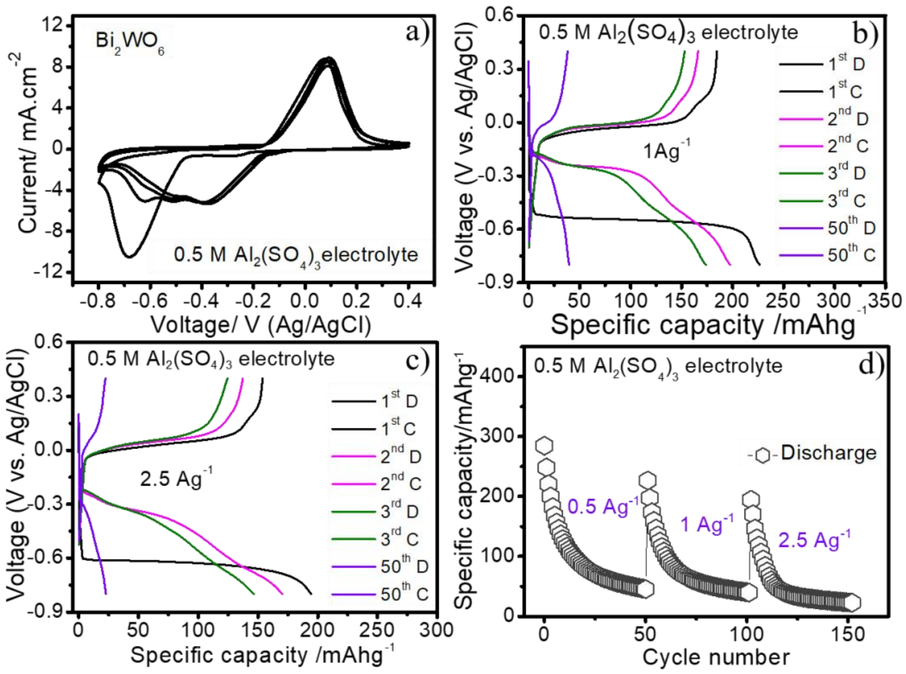

**Figure 4.8** Galvanostatic charge discharge profiles of $Bi_2WO_6$ at a current density of (a) 0.5 $Ag^{-1}$, (b) 1 $Ag^{-1}$ and c) 2.5 $Ag^{-1}$; c) Rate capability of $Bi_2MoO_6$ at different current densities in 0.5 M aqueous $Al_2(SO_4)_3$ electrolyte.

Figure 4.7a shows the CV profiles of $Bi_2WO_6$ in 1 M $AlCl_3$ electrolyte at a scan rate of 2.5 $mVs^{-1}$. In this case, two cathodic peaks of varying intensities could be noticed at -0.3 V and -0.67 V in the 1st cathodic scan, while there is only one anodic peak around 0.02 V. In subsequent cathodic cycles, a broad peak emerges in the potential range of -0.4 V to -0.8 V. This is again reflected in the charge-discharge profiles of $Bi_2WO_6$ in 1 M $AlCl_3$ aqueous electrolyte at a current rate of 0.5 $Ag^{-1}$ (figure 4.7b). There are two distinct discharge potential plateaus at -0.2 V and -0.4 V in the first discharge cycle with a concomitant charge plateau at -0.1 V. The initial discharge and charge capacities are estimated to be 257 $mAhg^{-1}$ and 140 $mAhg^{-1}$ respectively. Similar trend is also seen at higher current densities (figure 4.7c). However, all the measurements suffer from capacity decline (figure 4.7d). Electrochemical measurements were conducted again in 0.5 M $Al_2(SO_4)_3$ aqueous electrolyte (figure 4.8). As could be seen from the CV profiles (figure 4.8a), now there is a pair of prominent cathodic and anodic peaks around -0.4 V and -0.1 V respectively except the cathodic peak around -0.7 V in the first cycle. The charge-discharge profiles as shown in figure 4.8(b, c) are quite consistent with the CV profiles. The initial discharge and charge capacities are evaluated to be 284 $mAhg^{-1}$ and

225 mAhg$^{-1}$ at a current rate of 0.5 Ag$^{-1}$. After 50th cycle, the capacities are around 50 mAhg$^{-1}$ (figure 4.8d).

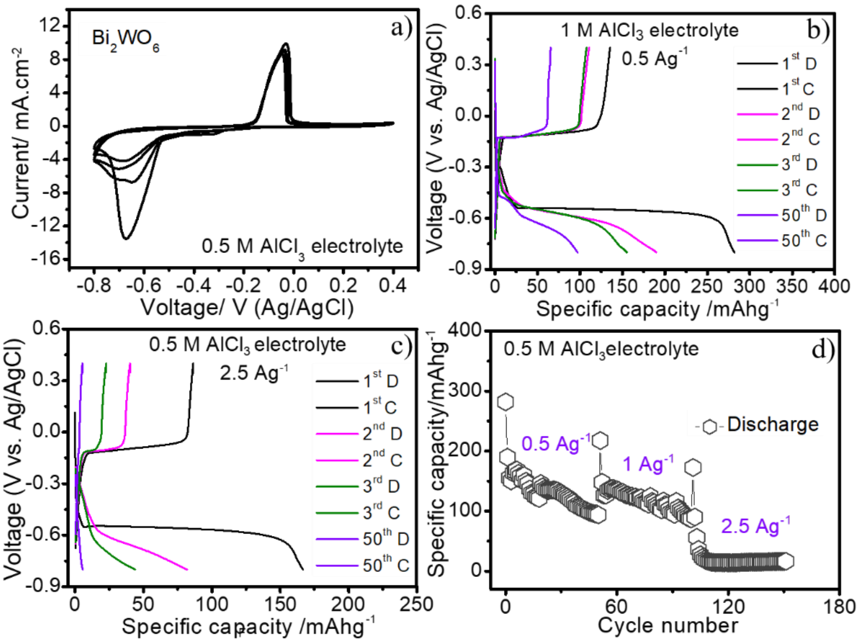

**Figure 4.9** Galvanostatic charge discharge profiles of $Bi_2WO_6$ at a current density of (a) 0.5 Ag$^{-1}$, (b) 1 Ag$^{-1}$ and c) 2.5 Ag$^{-1}$; c) Rate capability of $Bi_2WO_6$ at different current densities in 1 M aqueous $AlCl_3$ electrolyte.

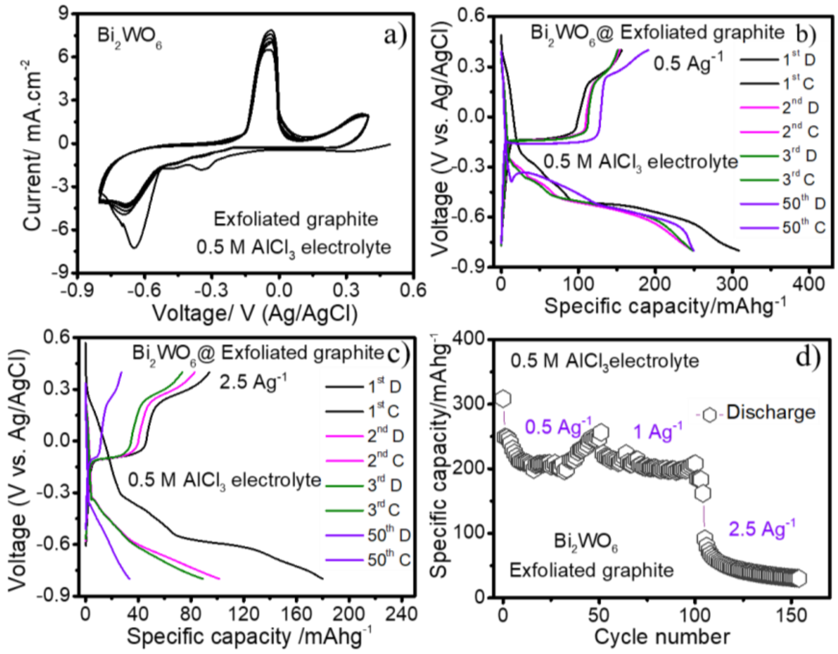

**Figure 4.10** Galvanostatic charge discharge profiles of $Bi_2WO_6$ at a current density of (a) 0.5 Ag$^{-1}$, (b) 1 Ag$^{-1}$ and c) 2.5 Ag$^{-1}$; (c) Rate capability of $Bi_2WO_6$ at different current densities in 0.5 M aqueous $AlCl_3$ electrolyte. Current collector used here is exfoliated graphite.

Figure 4.9a shows the CV profiles of $Bi_2WO_6$ in 0.5 M $AlCl_3$ aqueous electrolyte at a scan rate of 2.5 $mVs^{-1}$. In contrast to 1 M $AlCl_3$ electrolyte, only one pair of cathodic and anodic peaks is seen around -0.67 V and -0.03 V in all the scans which is again well corroborated with the charge-discharge profiles (figure 4.9b). However, as shown in figure 4.9(b-d), the capacity decline could be significantly impeded with the lower concentration of $AlCl_3$ aqueous electrolyte. The discharge and charge capacities are around 100 $mAhg^{-1}$ and 65 $mAhg^{-1}$ at the 50th cycle at a current rate of 0.5 $Ag^{-1}$ (figure 4.9b). Interestingly, this was not the case for $Bi_2MoO_6$ (figure 4.4). In an effort to further enhance the storage capacity and stability of $Bi_2WO_6$, charge-discharge experiments in 0.5 M $AlCl_3$ aqueous electrolyte were conducted using exfoliated graphite as the current collector (figure 4.10). The process of obtaining exfoliated graphite was described in our previous work [11]. It could be observed from figure 4.10(b-d) that there is significant improvement in storage capacity. A stable capacity above 200 $mAhg^{-1}$ is attained at a specific current rate of 0.5 $Ag^{-1}$ (figure 4.10b).

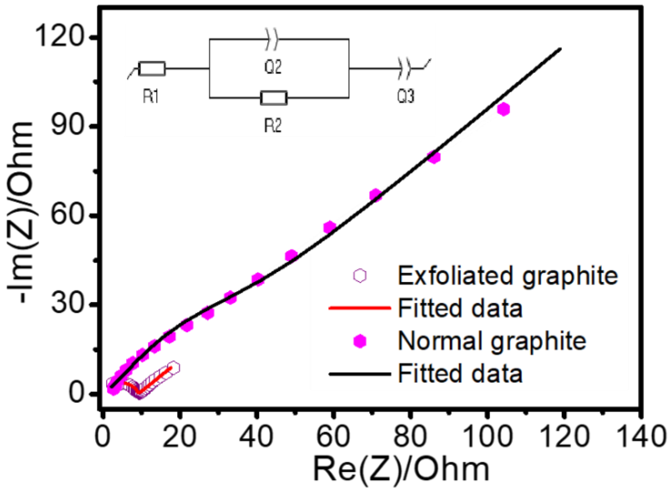

**Figure 4.11** EIS spectra of $Bi_2WO_6$ coated on normal and exfoliated graphite in 0.5 M $AlCl_3$.

| **Sl/No** | **Types of current collector** | **Charge transfer resistance ($R_2$) ($ohm.cm^{-2}$)** |
|---|---|---|
| 1 | Normal graphite | 12.11 |
| 2 | Exfoliated graphite | 9.039 |

**Table 4.1**: Charge transfer resistance values obtained from fitting the EIS data shown in previous figure

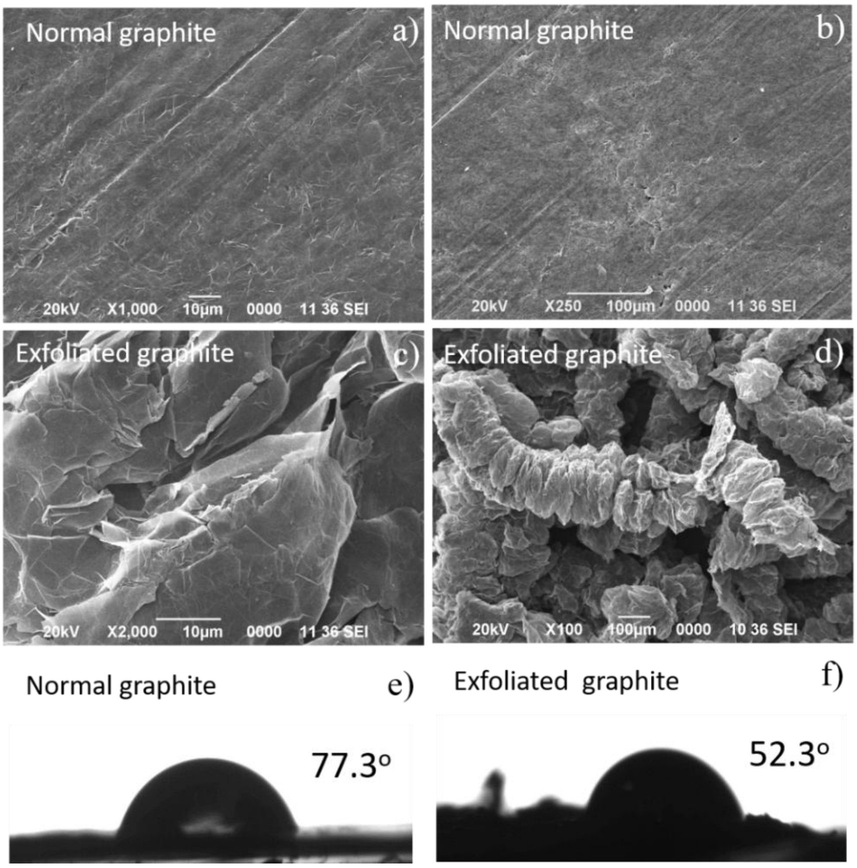

**Figure 4.12** SEM images of (a-b) normal graphite and (c-d) exfoliated graphite, contact angle measurements of (c) normal graphite and (f) exfoliated graphite.

Electrochemical impedance spectroscopy analysis of the electrodes in pristine graphite and exfoliated graphite indicates lower charge transfer resistance in the case of exfoliated electrode (figure 4.11 and Table 4.1). An examination of the surface of the normal graphite and exfoliated graphite from the obtained SEM images (figure 4.12 (a,b), (c,d)) hints that the surface of the normal graphite is almost smooth, whereas the exfoliated graphite resembles a porous structure made of nanosized graphite flakes. Therefore, it is expected that the number of channels for ion flux at any instant for the exfoliated graphite electrode is relatively higher in comparison to normal graphite electrode. This obviously influences the electrochemical activity. Additionally, the electrochemical exfoliation may facilitate inclusion of functional groups on the surface which may increase the hydrophilicity of the exfoliated graphite. It is supported by the contact angle measurement. As shown in figure 4.12(e,f), it is observed that the contact angle for exfoliated graphite (52.3°) is much lower than the normal graphite (77.3°). Hydrophobicity of the substrate is important in this case since the electrochemical evaluations are performed in aqueous medium.

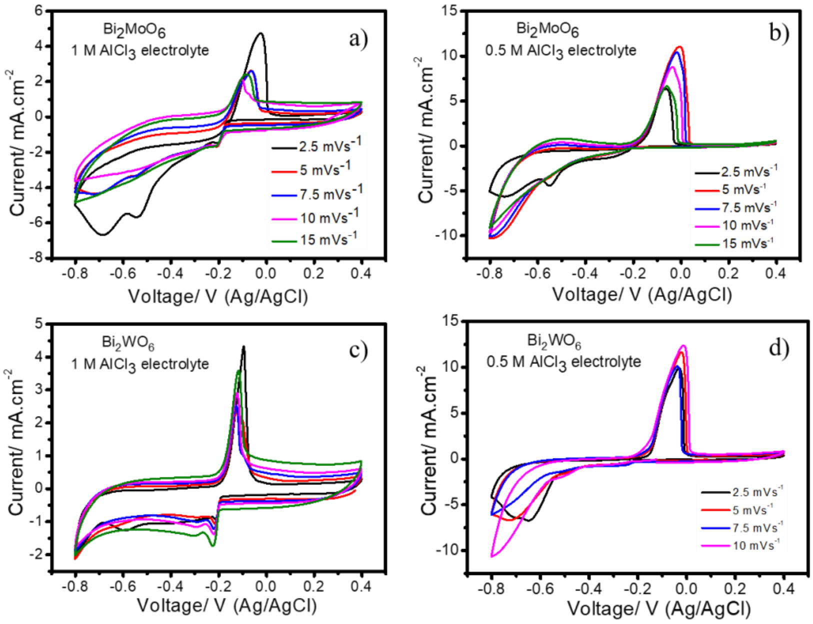

**Figure 4.13** CV profile of $Bi_2MoO_6$ at different scan rate in a) 1 M $AlCl_3$ and b) 0.5 M $AlCl_3$ aqueous electrolyte. CV profile of $Bi_2WO_6$ at different scan rate in a)1 M $AlCl_3$ and b) 0.5 M $AlCl_3$ aqueous electrolyte.

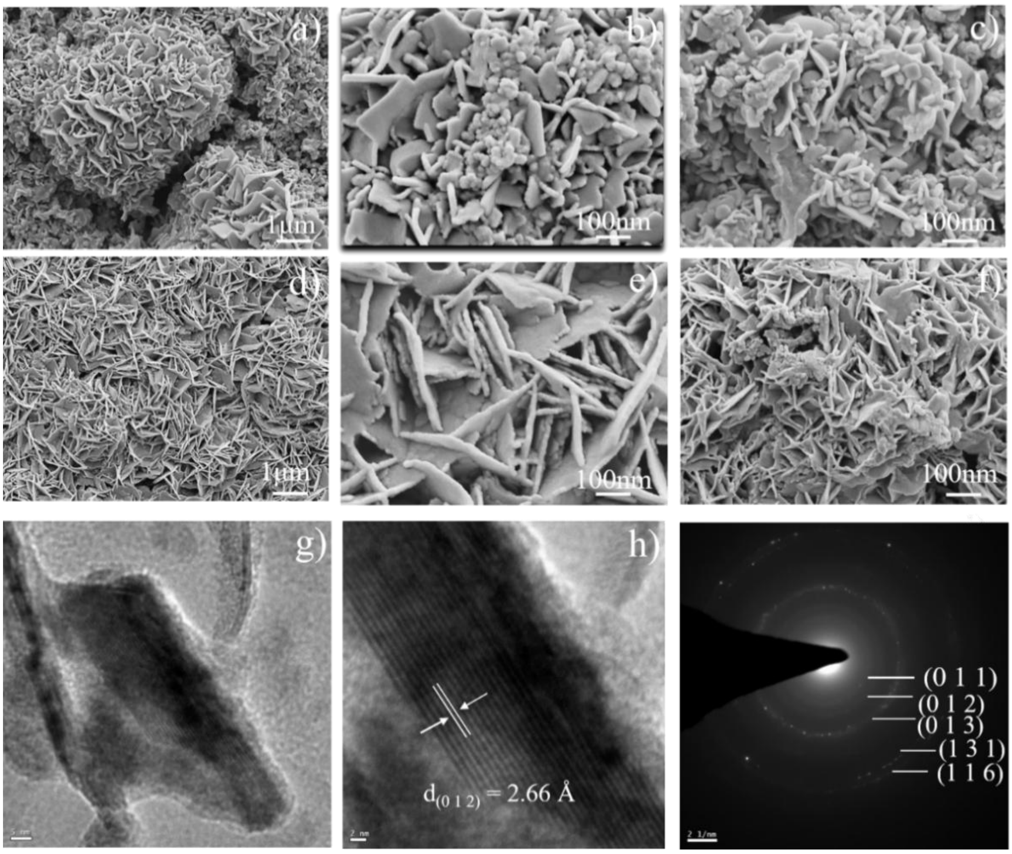

**Figure 4.14** Ex-situ FESEM images of $Bi_2WO_6$ after (a-c) 1st discharge, (d-f) 1st charge, (g,h) HRTEM images and (i) SAED patterns of $Bi_2WO_6$, after 1st discharge.

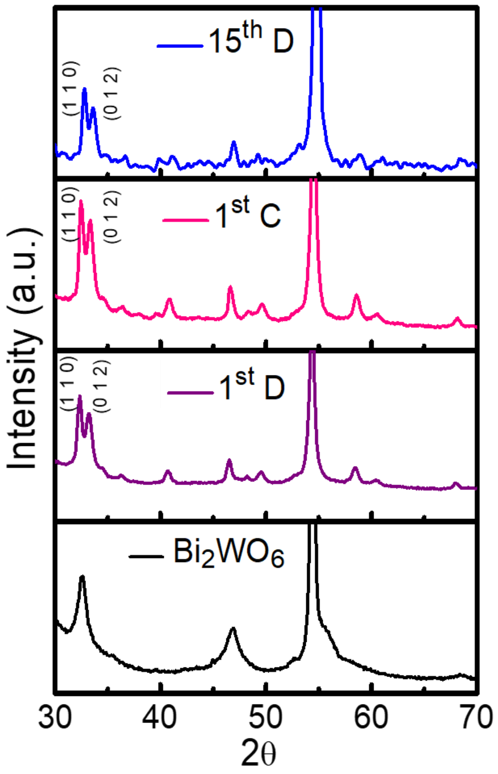

**Figure 4.15** Ex-situ XRD patterns of $Bi_2WO_6$ before and after 1st discharge, 1st charge and 15th discharge state, respectively.

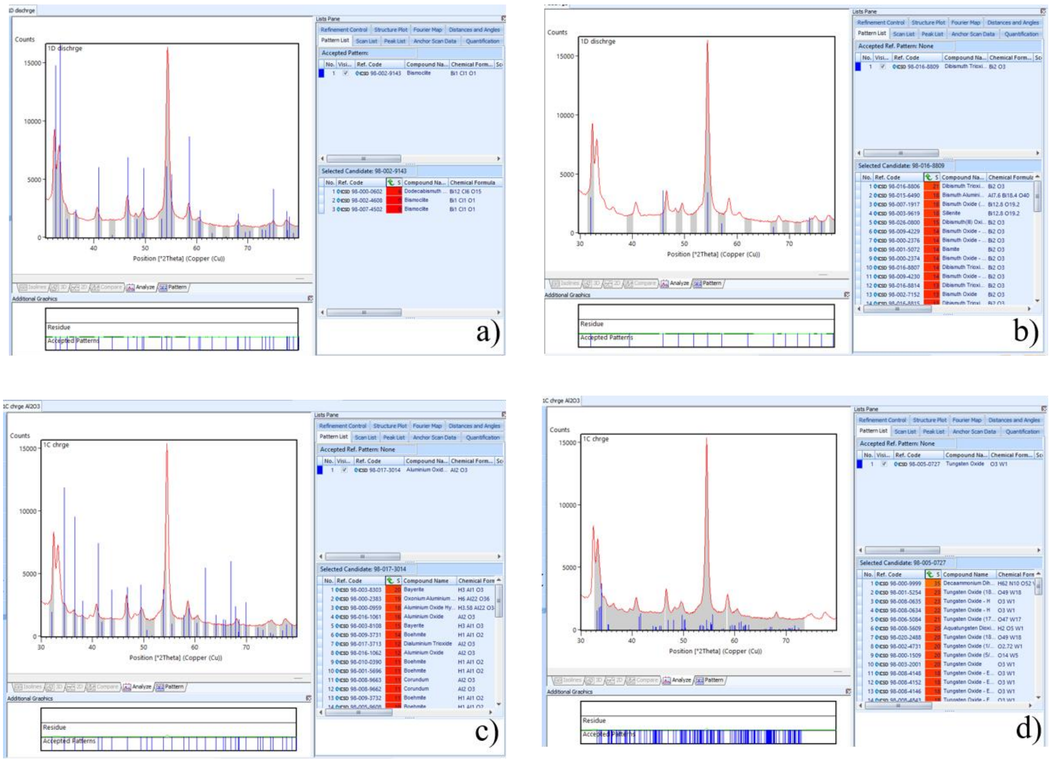

**Figure 4.16**: High score plus analysis of (a) BiOCl. (b) $Bi_2O_3$, (c) $Al_2O_3$ and (d) $WO_3$ of the discharged state electrode.

To understand the electrochemical $Al^{3+}$ ion storage mechanism in $Bi_2WO_6$, the discharged and charged state electrodes were analyzed by FESEM, HRTEM, XRD, XPS, Raman, FTIR, UV-Visible techniques. First of all, it is to be noted that the CV profiles obtained at different scan rates for $Bi_2WO_6/Bi_2MoO_6$ show that there is no direct relationship between the peak current and scan rate (figure 4.13). The ex-situ FESEM investigation indicates that the morphology of $Bi_2WO_6$ transforms from a closed packed morphology to a prominently visible two-dimensional open structure after the first discharge and charge (figure 4.14 (a-c), (d-f)). Ex-situ XRD patterns of the 1st discharged and 1st charged state electrodes (figure 4.15) were analyzed to identify the appearance of the probable crystal phases. It is clearly noticeable that the discharged state electrode contains few extra diffraction peaks in addition to $Bi_2WO_6$ peaks. For example, the peak positioned at $2\theta = 32.64^o$ splits into two peaks at $2\theta = 32.35^o$ and $2\theta = 33.37^o$. There is one new peak at $2\theta = 40.85^o$. There are three additional peaks between $2\theta = 45\text{-}50^o$ and two peaks between $2\theta = 58\text{-}62^o$. Almost similar pattern is observed for the 1st charged and 15th discharged state electrodes. The diffraction patterns are complex, however, most of the new peaks are similar to the BiOCl phase (ICSD no: 98-002-9143) (figure 4.16a). There is possibility of the presence of $Bi_2O_3$, $WO_3$ and $Al_2O_3$ phases which could not be properly identified due to the overlapping of the diffraction peaks (figure 4.16 (b-d)). The 1st discharge state electrode was further analysed by HRTEM and SAED. It could be seen from figure 4.14g that lamellar structure could be observed for the discharged electrode. In addition, a fringe spacing of 2.66 Å (figure 4.14h) is estimated which could be related to the (012) plane of BiOCl. Moreover, the SAED pattern (figure 4.14i) could also be mostly indexed to BiOCl phase (ICSD no: 98-002-9143).

Figure 4.17 shows the ex-situ XPS spectra of the $Bi_2WO_6$ electrode after 1st discharge and charge along with the XPS spectrum of the pristine $Bi_2WO_6$. The characteristic Bi 4f peaks for $Bi_2WO_6$ consist of two peaks namely Bi $4f_{7/2}$ and Bi $4f_{5/2}$ positioned at 159.8 eV and 165 eV respectively indicating a trivalent oxidation state for $Bi^{3+}$ (figure 4.15a) [12]. There is a minor shift (0.35 eV) in the peak positions after discharge and charge. Similarly, the peaks assigned for W also show a minor shift after cycling (figure 4.17b) [13]. On the other hand, the O 1s peak located at 530.6 eV, which can be assigned to the typical W-O bond, splits into two new peaks positioned at 530.4 eV and 532.4 eV after 1st discharge and 1st charge (figure 4.17c) [14]. In addition, The Cl 2p peak can be well observed at 198.76 eV (figure 4.17d). The binding energy ascribed to the $Cl2p_{3/2}$ can be well indexed with the Cl2p peak of BiOCl phase [15]. This gives an indication for the possible formation of BiOCl nanostructure from $Bi_2WO_6$ after subsequent cycling. The discharge and charge state of the $Bi_2WO_6$ electrodes also show the presence of Al 2p peak at 74.85 eV confirming the presence of Al (figure 4.17e) [16]. Figure 4.18a shows the comparison of Raman spectra of pristine $Bi_2WO_6$ and $Bi_2WO_6$ after subsequent cycling stage (e.g. 1st discharge, 1st charge and 15th discharge). All the characteristics Raman peaks of $Bi_2WO_6$ could be noticed in the pristine $Bi_2WO_6$ [17]. Notably, the peaks at 793 $cm^{-1}$ and 823 $cm^{-1}$ corresponds to the O-W-O symmetric and asymmetric vibration modes respectively, whereas the peak at 710 $cm^{-1}$ is related to the asymmetric stretching vibrations of W plane with O atoms in the W-O bond [18-20]. The peaks observed in the range of 250-350 $cm^{-1}$ corroborate the Bi-O bending vibrations at the top of the $WO_6$ octahedron. The peak around 150 $cm^{-1}$ is attributed to the external vibration of the $WO_6$ octahedron [21,22]. It is observed that the intensity of the $Bi_2WO_6$ characteristics peaks decreases after the 1st discharge/charge process and after 15th discharge cycle, most of the peaks almost disappeared. In addition, some of the peaks are either blue or red shifted. For example, the peak at 301 is blue shifted by 6 $cm^{-1}$ and the peak at 793 $cm^{-1}$ is red shifted by 4 $cm^{-1}$. It indicates the interaction of $Al^{3+}$ ion with $Bi_2WO_6$ crystal structure during the electrochemical process. It is also supported by the FTIR spectra of the discharged and charged state of the $Bi_2WO_6$ electrode (figure 4.18b) [23,24]. One of the characteristic peaks of $Bi_2WO_6$ i.e. the W-O stretching modes at 814 $cm^{-1}$ completely vanished after discharge/charge [25]. Whereas there is an emergence of a new prominent peak at 1113 $cm^{-1}$ which is related to Bi-Cl bond of BiOCl phase [26].

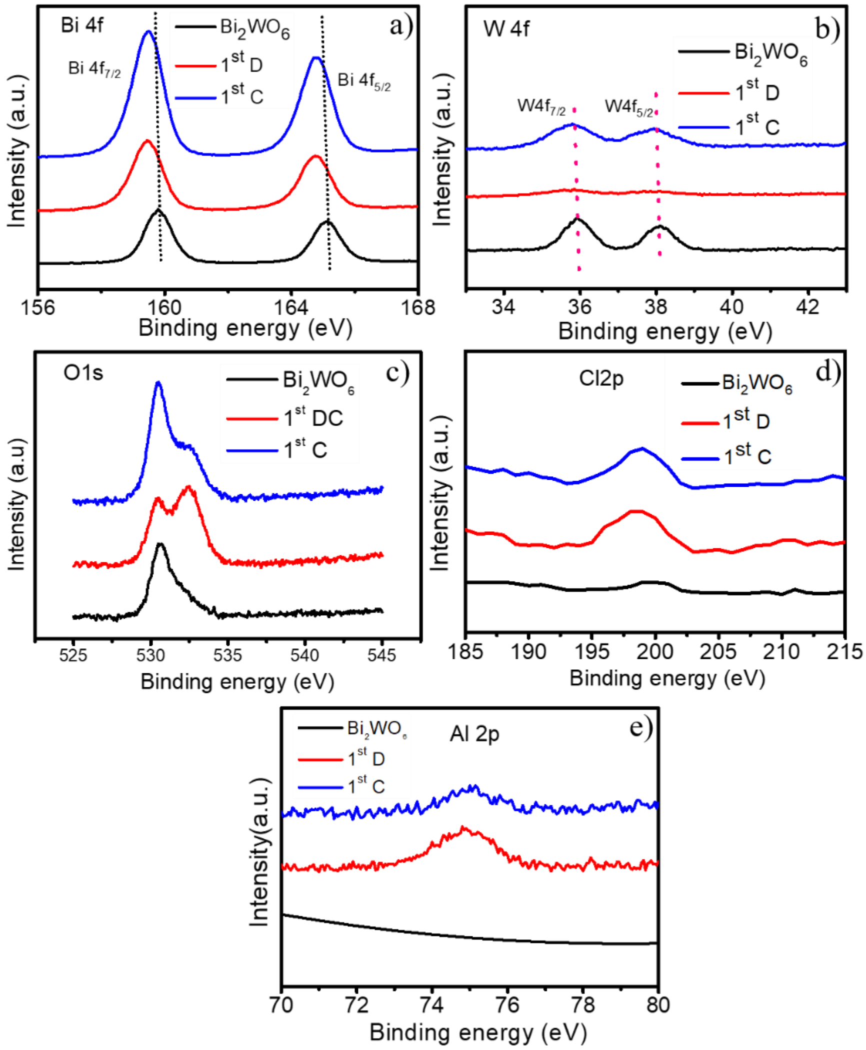

**Figure 4.17** Ex-situ XPS spectra of (a) Bi4f and (b) W4f, (c) O1s, (d) Cl2p and (e) Al2p of $Bi_2WO_6$ before and after 1st discharge, 1st charge and 15th discharge state, respectively.

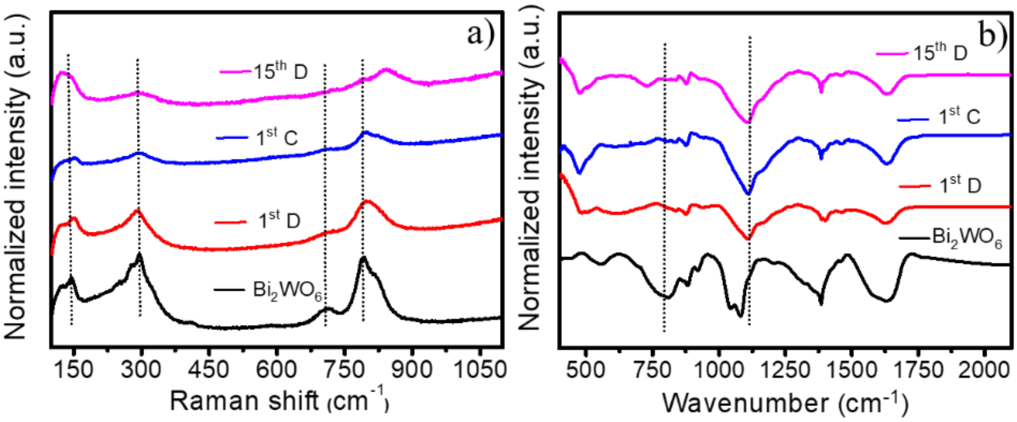

**Figure 4.18** (a) Raman spectra and (b) FTIR spectra of $Bi_2WO_6$ before and after 1st discharge, 1st charge and 15th discharge state, respectively.

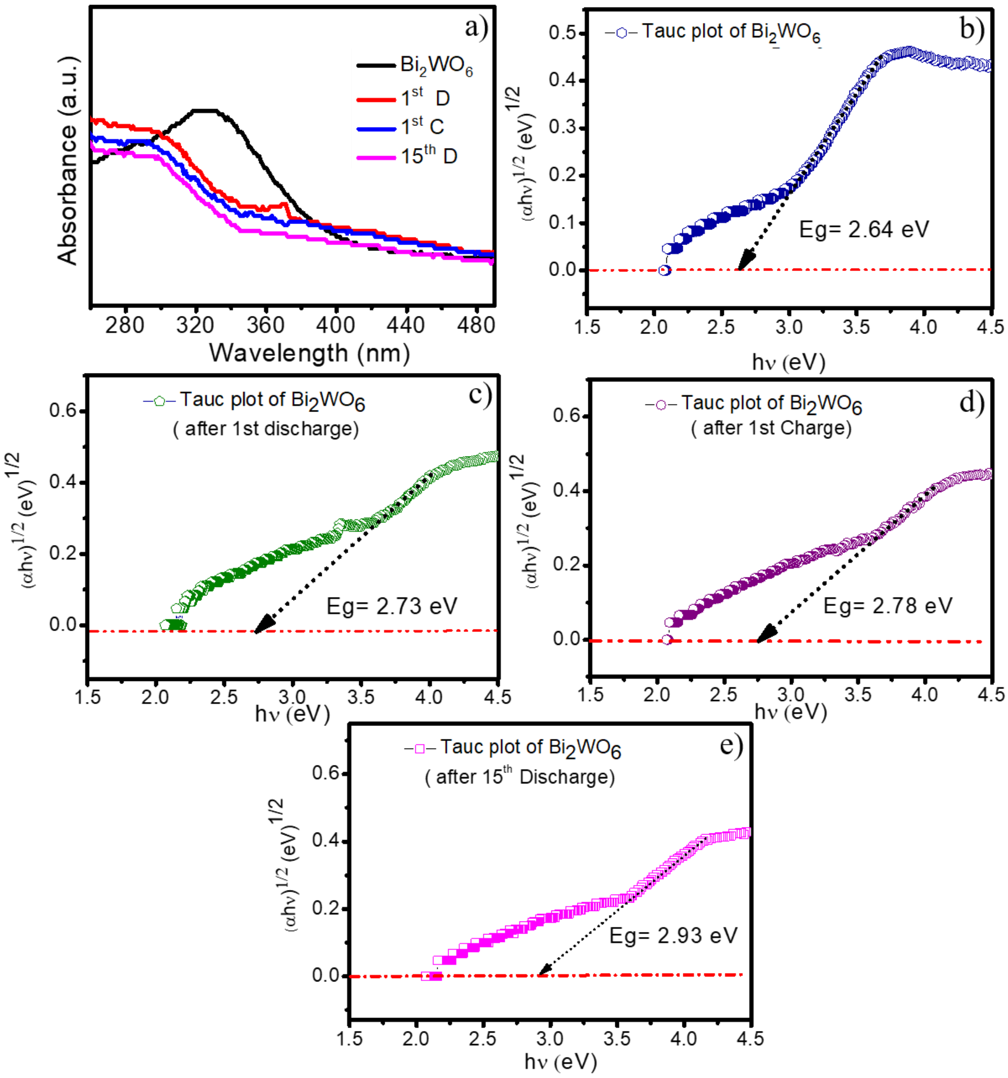

**Figure 4.19** (a) UV-visible spectra before and after cycling, Tauc plots (b) before cycling, (c) After 1st discharge, (d) after 1st charge and (e) after 15th discharge of $Bi_2WO_6$.

| Sl no | State of the material | Obtained band gap (in eV) |
|---|---|---|
| 1 | Pristine $Bi_2WO_6$ | 2.64 |
| 2 | After 1st discharge | 2.73 |
| 3 | After 1st charge | 2.78 |
| 4 | After 15th discharge | 2.93 |

**Table 4.2**: obtained band gap values. of $Bi_2WO_6$ before and after 1st discharge, 1st charge and 15th discharge state, respectively.

Ex-situ UV-visible spectral analysis also indicates a change in the structure of $Bi_2WO_6$ after cycling. Figure 4.19a shows the UV visible spectra of pristine $Bi_2WO_6$ and $Bi_2WO_6$ after subsequent cycling. In case of pristine $Bi_2WO_6$, an absorption edge around 450 nm could be noticed similar to previous reports [27]. However, a blue shift in the absorption edge is observed for the discharged/charged state electrode. Based on the UV-visible outcomes, the band gap energy values are calculated (figure 4.19 and Table 4.2) and it is found that there is slight increase in the band gap of the discharged/charged state electrodes in comparison to pristine $Bi_2WO_6$. Considering all of these outcomes, there are possibilities of two reaction mechanisms during the electrochemical process. First, since $Bi_2WO_6$ is a layered structure with $(Bi_2O_2)^{2+}$ sheets sandwiched by $(WO_4)^{2-}$ layers, the $Al^{3+}$ ion may get inserted inside the interlayers. Second, during the discharge-charge process, some of the $(Bi_2O_2)^{2+}$ sheets exposed to the electrolyte may react with the free $Cl^-$ ions in the electrolyte to form BiOCl. There are instances of leaching of $(Bi_2O_2)^{2+}$ to form bismuth oxyhalides in acidic environments [28]. Overall, it could be summarized as: (a) $Bi_2WO_6 + xAl^{3+} + xe^- \rightarrow (Bi_2O_2)^{2+}(xAl^{3+})\ (WO_4)^{2-}$ and (b) $Bi_2O_2 + 2Cl^- \rightarrow 2BiOCl + 2e^-$. It is to be noted here that this kind of phase change may result in not only low coulombic efficiencies but also can influence the first discharge profile. An analogous situation could be highlighted here as was illustrated by Tarascon and his coworkers in a study on transition metal oxides [29]. For example, when $Li^+$ ion reacted with CoO to form nanosized Co and $Li_2O$ in the 1st discharge cycle, the discharge profile was completely different from the rest of the cycles. Notably, there was a very flat discharge plateau in the 1st discharge cycle. Moreover, the Coulombic efficiency was also lowest for the first cycle.

## 4.4 Conclusion

In summary, this chapter illustrates the electrochemical behaviours of $Bi_2MoO_6$ and $Bi_2WO_6$ for $Al^{3+}$ ion storage in aqueous electrolyte. It is found that the electrochemical activities are different for different aqueous electrolytes for both the materials. Although capacity fading is a severe problem for both the materials in 1 M $AlCl_3$ aqueous electrolyte, the electrochemical stability could be seen for 0.5 M $AlCl_3$ aqueous electrolyte only for $Bi_2WO_6$. While the charge-discharge profiles are almost identical for both $Bi_2MoO_6$ and $Bi_2WO_6$, it is to be noted that $Bi_2WO_6$ exhibits better electrochemical long-term stability and severe capacity decline is noticeable for $Bi_2MoO_6$. The specific discharge capacity is 94 $mAhg^{-1}$ at a current density of 1 $Ag^{-1}$ over 50 cycles for $Bi_2WO_6$

in an optimized $AlCl_3$ aqueous electrolyte. The specific capacity could significantly be enhanced by the use of an exfoliated graphite current collector. The electrochemical impedance spectra (EIS) of natural and exfoliated graphite shows less charge transfer resistance in case of exfoliated graphite substrates which results in the improved electrochemical storage behavior of $Bi_2WO_6$. The mechanistic study suggests formation of BiOCl during the charge/discharge process.

## 4.5 References

[1] Zhang, L., Wang, H., Chen, Z., Wong, P.K. and Liu, J. $Bi_2WO_6$ micro/nano-structures: synthesis, modifications, and visible-light-driven photocatalytic applications. *Applied Catalysis B: Environmental*, 106(1-2): 1-13, 2011.

[2] Shinde, P.V., Shinde, N.M., Yun, J.M., Mane, R.S. and Kim, K.H. Facile chemical synthesis and potential supercapattery energy storage application of hydrangea-type $Bi_2MoO_6$. *ACS omega*, 4(6):11093-11102, 2019.

[3] Elaouni, A., El Ouardi, M., BaQais, A., Arab, M., Saadi, M. and Ahsaine, H.A. Bismuth tungstate $Bi_2WO_6$: a review on structural, photophysical and photocatalytic properties. *RSC advances*, 13(26):17476-17494,2023.

[4] Shi, Y., Feng, S. and Cao, C. Hydrothermal synthesis and characterization of $Bi_2MoO_6$ and $Bi_2WO_6$. *Materials Letters*, 44(3-4): 215-218, 2000.

[5] Li, S., Bai, L., Ji, N., Yu, S., Lin, S., Tian, N. and Huang, H. Ferroelectric polarization and thin-layered structure synergistically promoting $CO_2$ photoreduction of $Bi_2MoO_6$. *Journal of Materials Chemistry A*, 8(18): 9268-9277, 2020.

[6] Qin, Y., Liu, S., Shen, X., Gui, H. and Bai, Y. Enhanced gas sensing performance of $Bi_2MoO_6$ with introduction of oxygen vacancy: Coupling of experiments and first-principles calculations. *Journal of Alloys and Compounds*, 894: 162534, 2022.

[7] Tian, J., Sang, Y., Yu, G., Jiang, H., Mu, X. and Liu, H.A $Bi_2WO_6$-based hybrid photocatalyst with broad spectrum photocatalytic properties under UV, visible, and near-infrared irradiation. *Advanced Materials*, 25(36): 5075-5080, 2013.

[8] He, X., Chen, C., Gong, Y., Zeng, H. and Yi, Z. $Bi_2WO_6$ lead-free ferroelectrics: microstructure design, polar behavior and photovoltaic performance. *Journal of Materials Chemistry C*, 9(24):7539-7544.

[9] Qiao, Z., Liu, Z., Yan, W., Ruan, M., Guo, Z. and Wu, X.Pyro-photo-electric catalysis in $Bi_2WO_6$ nanostructures for efficient degradation of dyes under thermal-assisted visible light irradiation. *Journal of Alloys and Compound*s, 892: 162203, 2022.

[10] Yu, T., Li, Z., Chen, S., Ding, Y., Chen, W., Liu, X., Huang, Y. and Kong, F. Facile synthesis of flowerlike $Bi_2MoO_6$ hollow microspheres for high-performance supercapacitors. *ACS Sustainable Chemistry & Engineering*, 6(6): 7355-7361,2018.

[11] Nandi, S. and Das, S.K. Realizing a low-cost and sustainable rechargeable aqueous aluminum-metal battery with exfoliated graphite cathode. *ACS Sustainable Chemistry & Engineering*, 7(24): 19839-19847, 2019.

[12] Li, W., Xu, Y., Dong, Y., Wu, Y., Zhang, C., Zhou, M., Fu, Q., Wu, M. and Lei, Y. Bismuth oxychloride nanoflake assemblies as a new anode for potassium ion batteries. *Chemical Communications*, 55(46): 6507-6510, 2019.

[13] Minh Vuong, N., Kim, D. and Kim, H. Porous Au-embedded $WO_3$ nanowire structure for efficient detection of $CH_4$ and $H_2S$. *Scientific reports*, 5(1): 11040, 2015.

[14] Vasilopoulou, M., Soultati, A., Georgiadou, D.G., Stergiopoulos, T., Palilis, L.C., Kennou, S., Stathopoulos, N.A., Davazoglou, D. and Argitis, P. Hydrogenated under-stoichiometric tungsten oxide anode interlayers for efficient and stable organic photovoltaics. *Journal of Materials Chemistry A*, 2(6):1738-1749, 2014.

[15] Ding, L., Wei, R., Chen, H., Hu, J. and Li, J. Controllable synthesis of highly active BiOCl hierarchical microsphere self-assembled by nanosheets with tunable thickness. *Applied Catalysis B: Environmental*, 172: 91-99, 2015.

[16] Wu, C., Gu, S., Zhang, Q., Bai, Y., Li, M., Yuan, Y., Wang, H., Liu, X., Yuan, Y., Zhu, N. and Wu, F. Electrochemically activated spinel manganese oxide for

rechargeable aqueous aluminum battery. *Nature Communications*, 10(1): 73, 2019.

[17] Zhou, H., Wen, Z., Liu, J., Ke, J., Duan, X. and Wang, S. Z-scheme plasmonic Ag decorated $WO_3/Bi_2WO_6$ hybrids for enhanced photocatalytic abatement of chlorinated-VOCs under solar light irradiation. *Applied Catalysis B: Environmental*, 242: 76-84, 2019.

[18] Wang, R., Jiang, Z., Xu, L. and Liu, C. Synthesis of Dy (III) doped $Bi_2WO_6$ photocatalyst with highly efficient photocatalytic performance under simulated sunlight. *Journal of Materials Science: Materials in Electronics*, 32: 6931-6941, 2021.

[19] Huang, Y., Kou, S., Zhang, X., Wang, L., Lu, P. and Zhang, D. Facile fabrication of Z-scheme $Bi_2WO_6/WO_3$ composites for efficient photodegradation of bisphenol A with peroxymonosulfate activation. *Nanomaterials*, 10(4): 724, 2020.

[20] Xing, Z., Hu, J., Ma, M., Lin, H., An, Y., Liu, Z., Zhang, Y., Li, J. and Yang, S. From one to two: in situ construction of an ultrathin 2D-2D closely bonded heterojunction from a single-phase monolayer nanosheet. *Journal of the American Chemical Society*, 141(50):19715-19727, 2019.

[21] Dumrongrojthanath, P., Saksoong, T., Patiphatpanya, P., Phuruangrat, A., Thongtem, S. and Thongtem, T. Microwave-assisted hydrothermal synthesis of $BiOCl/Bi_2WO_6$ nanocomposites for the enhancement of photocatalytic efficiency. *Research on Chemical Intermediates*, 45: 2301-2312, 2019.

[22] Liang, Y. and Shi, J. Effect of halide ions on the microstructure of $Bi_2WO_6$ with enhanced removal of rhodamine B. *Journal of Inorganic and Organometallic Polymers and Materials*, 30(8): 2872-2880, 2020.

[23] Huang, Y., Kou, S., Zhang, X., Wang, L., Lu, P. and Zhang, D. Facile fabrication of Z-scheme $Bi_2WO_6/WO_3$ composites for efficient photodegradation of bisphenol A with peroxymonosulfate activation. *Nanomaterials*, 10(4): 724, 2020.

[24] Zhu, T., Hou, Y., Huang, G., Fu, T., Yang, J., Wang, Y. and Zhang, H. Dual modification based on electrostatic repulsion of bentonite and SPR effect of Bi facilitate charge transfer of $Bi_2WO_6$ for antibiotics degradation. *Environmental Science and Pollution Research*, 30(11): 28874-28888, 2023.

[25] Zhao, G., Liu, S., Lu, Q. and Song, L. Controllable synthesis of $Bi_2WO_6$ nanofibrous mat by electrospinning and enhanced visible photocatalytic degradation performances. *Industrial & engineering chemistry research*, 51(31): 10307-10312, 2012.

[26] Tang, W., Zhang, Y., Guo, H. and Liu, Y. Heterogeneous activation of peroxymonosulfate for bisphenol AF degradation with $BiOI_{0.5}Cl_{0.5}$. *RSC advances*, 9(25):14060-14071,2019.

[27] Huang, Y., Yin, X., He, P., Kou, S., Zhang, X., Wang, L. and Lu, P. Peroxymonosulfate activation by $Bi_2WO_6$/BiOCl heterojunction nanocomposites under visible light for bisphenol A degradation. *Nanomaterials*, 11(11): 3130, 2021.

[28] Gnayem, H. and Sasson, Y., 2013. Hierarchical nanostructured 3D flowerlike $BiOCl_xBr_{1-x}$ semiconductors with exceptional visible light photocatalytic activity. *ACS catalysis*, 3(2):186-191, 2013

[29] Poizot, P.L.S.G., Laruelle, S., Grugeon, S., Dupont, L. and Tarascon, J.M. Nano-sized transition-metal oxides as negative-electrode materials for lithium-ion batteries. *Nature*, 407(6803): 496-499, 2000.